

Efficient Robust Design for Thermoacoustic Instability Analysis: A Gaussian Process Approach

Shuai Guo¹

Professur für Thermofluidynamik,
Technische Universität München,
Boltzmannstr. 15,
Garching D-85748, Germany
e-mail: guo@tfd.mw.tum.de

Camilo F. Silva

Professur für Thermofluidynamik,
Technische Universität München,
Boltzmannstr. 15,
Garching D-85748, Germany
e-mail: silva@tfd.mw.tum.de

Wolfgang Polifke

Professur für Thermofluidynamik,
Technische Universität München,
Boltzmannstr. 15,
Garching D-85748, Germany
e-mail: polifke@tum.de

In the preliminary phase of analyzing the thermoacoustic characteristics of a gas turbine combustor, implementing robust design principles is essential to minimize detrimental variations of its thermoacoustic performance under various sources of uncertainties. In this study, we systematically explore different aspects of robust design in thermoacoustic instability analysis, including risk analysis, control design, and inverse tolerance design. We simultaneously take into account multiple thermoacoustic modes and uncertainty sources from both the flame and acoustic boundary parameters. In addition, we introduce the concept of a “risk diagram” based on specific statistical descriptions of the underlying uncertain parameters, which allows practitioners to conveniently visualize the distribution of the modal instability risk over the entire parameter space. Throughout this study, a machine learning method called “Gaussian process” (GP) modeling approach is employed to efficiently tackle the challenge posed by the large parameter variational ranges, various statistical descriptions of the parameters, as well as the multifaceted nature of robust design analysis. For each of the investigated robust design tasks, we propose an efficient solution strategy and benchmark the accuracy of the results delivered by GP models. We demonstrate that GP models can be flexibly adjusted to various tasks while only requiring one-time training. Their adaptability and efficiency make this modeling approach very appealing for industrial practices. [DOI: 10.1115/1.4044197]

1 Introduction

The occurrence of thermoacoustic instability [1] during the operation of a gas turbine combustor constitutes one of the major concerns for aircraft engine manufacturers due to its catastrophic effect on the structural integrity of the combustor system as well as the life-span of the gas turbine. In practice, there are two facts that must be taken into account when designing the thermoacoustic characteristics of the combustor: First of all, the thermoacoustic behavior of the combustor is highly sensitive to small parameter variations in operating conditions as well as acoustic boundary conditions [2]; Second, uncertainties in those parameters are always present during actual combustor operation, i.e., those parameters will display stochastic features instead of staying at some fixed and predetermined nominal values. In consequence, the performance of the combustor may deteriorate once the key parameters controlling the thermoacoustic interaction of the system deviate from their respective nominal conditions, and in extreme cases, a combustor that is stable at nominal operational condition may become unstable under the influence of the stochastic parameter fluctuations. Therefore, implementing the framework of probabilistic system modeling and the principle of robust design are essential to minimize the impact of operational uncertainties on the thermoacoustic performance of the combustor, thus eliminating the costly design iterations, mitigating the operational risk, and promoting an overall more reliable and competitive gas turbine product.

Robust design is generally recognized as the process of carefully selecting design parameter values such that the system behavior is insensitive to various sources of uncertainties [3], which include operation condition uncertainty, actuator imprecision, modeling error, etc. Within the scope of stochastic optimization, uncertain parameters are modeled as random variables with

predefined joint probability distributions, and the robust design problem is usually cast as a two-level nested optimization problem [4]: the outer loop forms a conventional optimization problem where an optimization algorithm is employed to find the design parameters that optimize the objective function while subjected to constraint functions. For each iteration, the inner loop is called where an uncertainty quantification (UQ) analysis is performed to calculate the uncertainty measures (e.g., mean, standard deviation, quantiles, etc.) of the system outputs given various sources of uncertainty, and those uncertainty measures are fed back to the outer loop to construct the corresponding objective and constraint functions. Overall, robust design can be viewed as the integration of optimization and UQ analysis.

In the context of thermoacoustic instability analysis, pioneer works were dedicated either to stabilize thermoacoustic modes via configuration optimization or to assess the variability of modal growth rate via UQ analysis. Regarding optimization, for example, Bade et al. [5] proposed a design for thermo-acoustic stability procedure, which optimizes geometric design parameters such that the annular combustor is stable, using network models and flame dynamic models derived from test rig data [6]. In addition, the recent work of Aguilar and Juniper [7] has proposed an adjoint-augmented optimization routine, which is capable of stabilizing all thermoacoustic modes of an annular combustor with minimum geometric modification. Regarding UQ analysis, different techniques have been proposed (i.e., analytical method [8], regression [9], adjoints [10–12], active subspace [8,13], polynomial chaos expansion [14,15]), to address the impact of various uncertainty sources (i.e., flame model, acoustic boundary condition, operation condition) on the variation of modal growth rate.

Despite the remarkable progress made in terms of optimization strategy as well as accelerating the UQ analysis, an integration of these two aspects into the robust design framework is, unfortunately, not straightforward and worth further investigation. Generally, an efficient robust design strategy poses more strict requirements on the perspective of UQ technique: First of all, the robust design problem encountered in thermoacoustic analysis

¹Corresponding author.

Manuscript received July 1, 2019; final manuscript received July 2, 2019; published online February 14, 2020. Editor: Jerzy T. Sawicki.

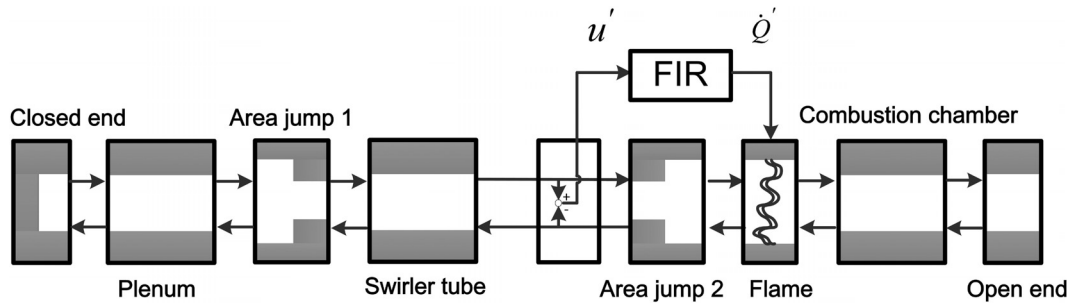


Fig. 1 Sketch of acoustic network model, flow from left to right

belongs to the “reliability-based” type [16], i.e., the constraint or objective is defined on the percentile of the modal growth rate distribution, rather than simply defined on its mean and standard deviation. As a consequence, UQ methods, which only provide mean and variance estimation, are no longer sufficient. Instead, a full probability density function (PDF) calculation of the modal growth rate is mandatory within each optimization iteration; second, the UQ technique has to be able to accommodate large parameter variation ranges so that optimization routines can fully explore different parameter combinations, thus having a better chance to locate the global optimum. And finally, the UQ technique has to be flexible enough to handle different types of PDFs associated with uncertain parameters, due to the fact that our knowledge regarding the uncertain parameters may be renewed as the design process evolves. In a word, robust design poses a serious challenge on the employed UQ strategy. To our best knowledge, no attempt has been made to integrate UQ analysis and optimization into the framework of robust design in thermoacoustic instability analysis.

The main objective of our current work is to explore this uncharted area via a machine learning method called Gaussian process (GP) modeling [17], which trains a computationally efficient surrogate model (GP model) to approximate the thermoacoustic solver. The novelties of our current work can be summarized as follows: first, for the first time we systematically investigate potential scenarios in pursuing the robust combustor thermoacoustic design. Those aspects of robust thermoacoustic design possess great significance in mitigating the operational risk of a gas turbine, yet have not received enough attention in the thermoacoustic research community; second, we identify different robust design tasks and properly categorize them as *risk analysis*, *design control*, and *inverse tolerance design*. In addition, we introduce the concept of a *risk diagram* as a high-level summary for all the investigated robust design tasks, which allows practitioners to conveniently visualize the distribution of the thermoacoustic instability risk over the entire parameter space, thus assisting optimum search performed in various robust design tasks. Third, for each identified robust design task, we not only provide rigorous mathematical formulations but also demonstrate how to exploit Gaussian process models to construct efficient solution strategy. Finally, we prove the capability of the GP modeling approach in significantly reducing the overall robust analysis time as well as flexibly coping with the multifaceted nature of the robust design process, both of which are highly favored by the industrial practices. We emphasize that, due to its “black-box” and “surrogate” nature, GP approach can make use of more sophisticated thermoacoustic and flame models than the ones used in the present work to investigate more complex combustors. Additionally, other aspects of robust design problems can be freely proposed and efficiently answered, all under one modeling framework, as will be demonstrated in our current paper.

This paper is organized as follows: Sec. 2 outlines the investigated combustor configuration, thermoacoustic modeling strategy, and the flame model. Section 3 specifies the uncertain parameters, thermoacoustic modes under consideration, and describes the

individual task we propose to address. Section 4 briefly overviews the fundamental theory of GP modeling methodology and presents detailed GP model training processes. A comparison between GP approach and other UQ methods is discussed at the end. Section 5 exploits the newly trained GP models in addressing each of the proposed robust design problem. The paper closes with the main conclusions.

2 Thermoacoustic Framework

This section starts with an introduction of the investigated test rig and the employed thermoacoustic modeling approach, followed by a description of the adopted flame dynamic response model, which will be embedded into the thermoacoustic modeling approach to calculate the eigen-frequencies and growth rates of the thermoacoustic modes.

2.1 Combustor Configuration. The BRS combustor configuration is investigated in this study, which represents a turbulent premixed swirl burner test rig [18,19]. The configuration consists of a plenum, a duct with an axial swirl generator, and a combustion chamber. In this study, an equivalence ratio of 0.77 of perfectly premixed methane–air mixture and a thermal power of 30 kW are considered as the operation conditions.

2.2 Thermoacoustic Modeling. In this study, a low-order acoustic network model is employed to calculate the eigen-frequencies and growth rates of the thermoacoustic modes. Figure 1 displays the network model representation of the burner test rig. Geometrical and thermodynamic parameters used in the acoustic network model are the same as Ref. [8], except the length of the combustor chamber is 0.75 m, and the reflection coefficient at the combustor exit is $|R_{out}|e^{i\tau}$ in the current study. Other modeling details can be found in Ref. [8] as well. It is worth mentioning that we adopt a rather simple yet practical acoustic network model in the current study only for the purpose of facilitating the benchmark of the robust design results. However, due to the nonintrusive nature of the GP modeling technique, which we discuss in Sec. 4, our proposed strategy can also be extended to more computational intensive acoustic models, e.g., Helmholtz equation, Linearized Navier–Stokes equation, etc., where the benefits of the GP approach could be further amplified, leveraging on the high accuracy of thermoacoustic modeling offered by the sophisticated solvers.

2.3 Flame Model. A flame dynamic response model similar to the distributed time lag model proposed by Komarek and Polifke [18] and validated by Oberleithner and Paschereit [20] is adopted in this study. This model determines the coefficients of the flame impulse response (FIR) by taking into account the flame response to both swirl number fluctuations and axial velocity fluctuations.

This model assumes that the shape of the flame impulse response can be approximated by adding three Gaussian

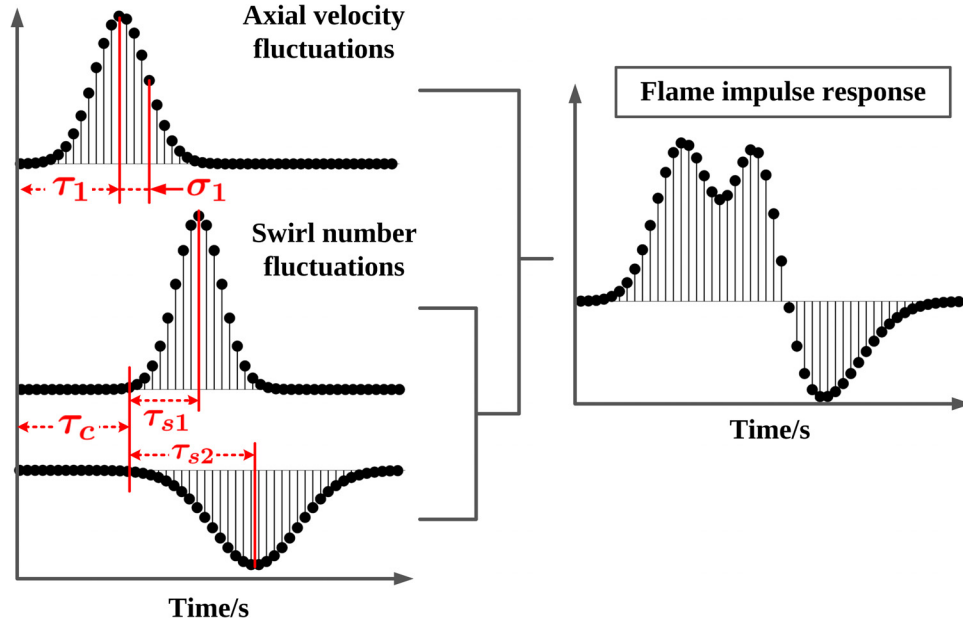


Fig. 2 Sketch of the employed FIR model for the flame dynamics. Corresponding frequency response is shown in Fig. 3(b).

distributions: one positive (+) Gaussian to account for the flame response to axial velocity fluctuations, and one (+) combined with another (−) Gaussian to describe the response to swirl number fluctuations.

An illustration of the flame model is given in Fig. 2, where its five model parameters, i.e., τ_1 , σ_1 , τ_c , τ_{s1} , τ_{s2} , are also shown. This parametrization is slightly different from Ref. [18] due to the following reasons: First, we want to explicitly express the time lag τ_c , which, according to the recent work of Albayrak and Polifke [21], represents the time needed for an inertial wave to propagate from the swirler to the flame base. Komarek and Polifke [18] have shown that the position of swirler can be changed without changing the mean flame shape and the flame response to axial velocity (τ_1 , σ_1) or swirl perturbations (τ_{s1} , τ_{s2}). Therefore, τ_c can be perceived as a control parameter to stabilize the combustor; second, this parametrization allows the introduction of flame parameter uncertainty while preserving the continuous shape of the flame impulse response. The remaining parameters are: τ_1 and σ_1 represent the mean and standard deviation of the flame heat release response under an impulse axial velocity perturbation, respectively; τ_{s1} and τ_{s2} represent the characteristic time lags for the flame response to the swirl number fluctuations. The standard deviations of the associated positive and negative Gaussian functions are considered to be one third of τ_{s1} and τ_{s2} , respectively. Therefore, we can express the value of the FIR coefficient h_k as [18]

$$h_k = \frac{\Delta t}{\sigma_1 \sqrt{2\pi}} e^{-\frac{(k\Delta t - \tau_1)^2}{2\sigma_1^2}} + \frac{\Delta t}{\sigma_2 \sqrt{2\pi}} e^{-\frac{(k\Delta t - \tau_2)^2}{2\sigma_2^2}} - \frac{\Delta t}{\sigma_3 \sqrt{2\pi}} e^{-\frac{(k\Delta t - \tau_3)^2}{2\sigma_3^2}} \quad k \in [1, 2, \dots, N] \quad (1)$$

where N is the number of FIR coefficients, and

$$\begin{aligned} \tau_2 &= \tau_c + \tau_{s1} & \tau_3 &= \tau_c + \tau_{s2} \\ \sigma_2 &= \tau_{s1}/3 & \sigma_3 &= \tau_{s2}/3 \end{aligned} \quad (2)$$

3 Robust Design Tasks

In this section, the investigated parameters as well as their variational ranges are introduced. Subsequently, two thermoacoustic modes are specified, which the following robust design analysis

will focus on. Afterward, detailed descriptions of our proposed design tasks are provided.

3.1 Uncertain Parameters. Our proposed robust design tasks involve six parameters, including five flame model parameters τ_1 , σ_1 , τ_c , τ_{s1} , τ_{s2} , and one acoustic boundary condition, i.e., the magnitude of the reflection coefficient at the combustor outlet $|R_{out}|$. Their nominal values (obtained from “Table 2, 30 kW optimal fit” in Ref. [22]) as well as their investigated variational ranges are summarized in Table 1. For τ_c and $|R_{out}|$, relatively large variational ranges are investigated in order to fully explore the parameter space. In a practical scenario, τ_c is determined by the distance between the swirler and the flame base [22], while the modification of $|R_{out}|$ can represent the installation of acoustic damping devices or a change of turbine working condition [23].

In our current study, three distribution types for τ_1 , σ_1 , τ_{s1} , τ_{s2} , are considered: independent uniform, independent Gaussian, and correlated Gaussian. As we stated in Sec. 1, a common situation in the design process is that our knowledge regarding the uncertain parameters may be renewed as the design process evolves. Here, independent uniform indicates the least informative knowledge, i.e., uncertain parameters have equal chance to be anywhere within the variational ranges. This usually happens at the beginning stage when no prior knowledge exists; Independent Gaussian contains more information since we know uncertain parameters have a tendency to appear more frequently around their corresponding mean; Correlated Gaussian, on the other hand, gives the most complete statistical description of the uncertain parameters. This usually happens at a later design stage when a sufficient

Table 1 Uncertainty information of the investigated parameters

| Parameters | | Nominal | Range |
|-------------------|-------------|---------------------|-----------------------------------|
| Flame (units: ms) | τ_1 | $\tau_1^0 = 2.85$ | $0.9\tau_1^0 - 1.1\tau_1^0$ |
| | σ_1 | $\sigma_1^0 = 0.7$ | $0.9\sigma_1^0 - 1.1\sigma_1^0$ |
| | τ_c | $\tau_c^0 = 3$ | 2–4.8 |
| | τ_{s1} | $\tau_{s1}^0 = 1.8$ | $0.9\tau_{s1}^0 - 1.1\tau_{s1}^0$ |
| | τ_{s2} | $\tau_{s2}^0 = 1.8$ | $0.9\tau_{s2}^0 - 1.1\tau_{s2}^0$ |
| Acoustic BC | $ R_{out} $ | $ R_{out} ^0 = 0.9$ | 0.6–1 |

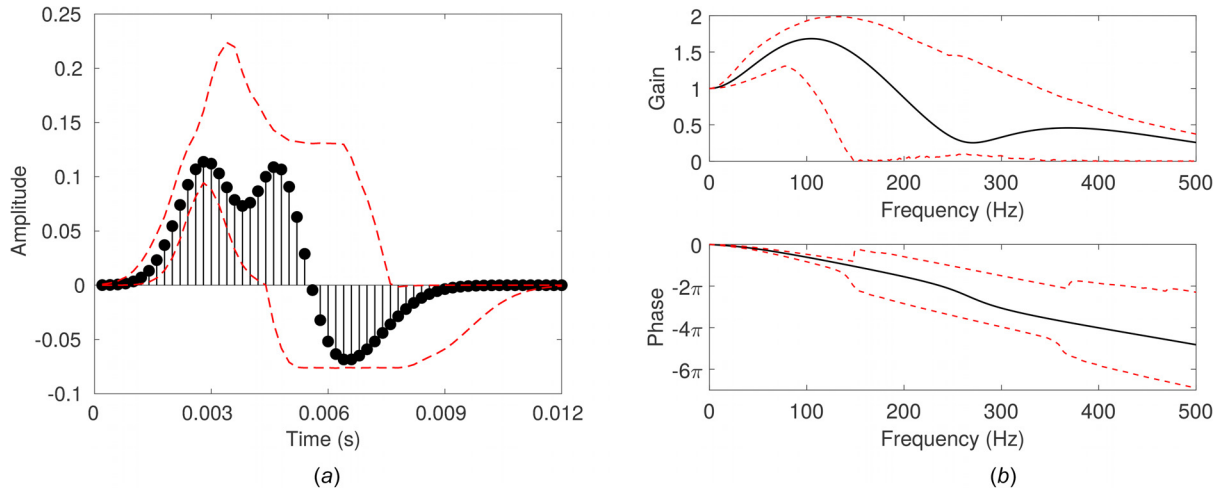


Fig. 3 Uncertainty reflected in FIR and FTF. The black stems represent the nominal values, while the red dash lines represent the envelopes recording the extreme values at each (a) coefficient h_k (FIR) and (b) frequency (FTF).

amount of experiments and simulations have been conducted so that the flame dynamics can be properly described. In Sec. 5, we start by considering τ_1 , σ_1 , τ_{s1} , τ_{s2} following independent uniform distribution, and then we assess the impact of different distribution types on the analysis results, all using the same GP models.

The uncertainties embedded in the flame model parameters can be easily propagated to the uncertainties in FIR coefficient h_k 's and the corresponding flame transfer function (FTF) by performing Monte Carlo on Eq. (1) and subsequently on Eq. (3). The uncertainty propagation results are shown in Fig. 3

$$\text{FTF}(\omega) = \sum_{k=1}^N h_k e^{-ik\Delta t\omega}, \quad \omega \in \mathbb{R} \quad (3)$$

3.2 Thermoacoustic Modes Specification. Figure 4 shows the thermoacoustic modes up to 400 Hz, calculated by deterministic analysis, i.e., when the nominal values of the flame model parameters and $|R_{\text{out}}|$ are used in the acoustic network. Highly damped modes are ignored; thus they are not shown in the figure. Two dominant thermoacoustic modes are presented: the higher frequency mode ($\omega = 287.5$ Hz, $\alpha = -27.7$ rad/s) is identified as the quarter wave mode of the combustor [19]. We denote this mode as *cavity mode*. The other mode ($\omega = 139.3$ Hz, $\alpha = -24.8$ rad/s) is identified as the intrinsic thermoacoustic mode (ITA) [24–26]. We denote this mode as *ITA mode*. Although both modes are not immediately adjacent to the stability limit, considering the large variational ranges of the FIR and FTF (displayed in Fig. 3), there still exists risk for both modes to be unstable. Also notice that it is not uncommon that in thermoacoustic control, the effort to stabilize one mode may unexpectedly promote another mode to become unstable [1]. Therefore, in our current study, both modes will be taken into account concurrently, and the goal of robust design analysis is to mitigate the risk of instability for both modes.

3.3 Design Task Descriptions. To comprehensively investigate the problem of robust thermoacoustic design, we propose the following scenarios, which we want to address individually:

Q1-Risk analysis: what are the *risk factors* [8] of the thermoacoustic modes of the system when uncertainties are presented in the flame parameter τ_1 , σ_1 , τ_{s1} , and τ_{s2} ?

Q2-Ideal control design: using τ_c as a control factor, what is the required minimum modification of τ_c to eliminate the risk of instability of both cavity and ITA mode simultaneously?

Q3-Realistic control design: in reality, we cannot perfectly control τ_c . Meanwhile, $|R_{\text{out}}|$ is also uncertain. How would these

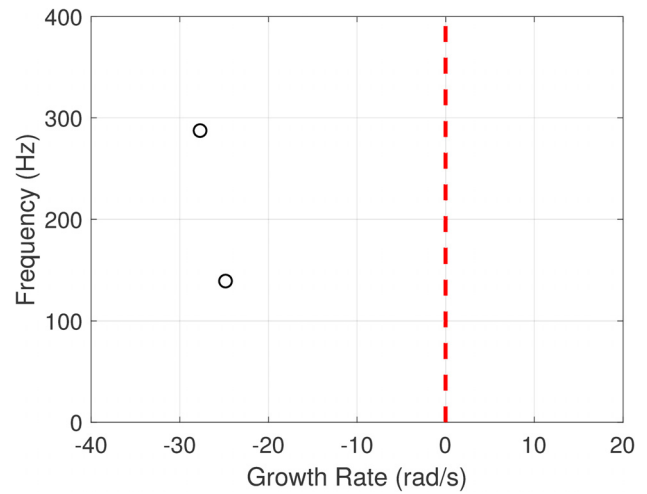


Fig. 4 Two dominant eigenmodes from deterministic analysis. In this study, modes with growth rates smaller than zero are considered stable.

two additional uncertain parameters affect the decision made from Q2?

Q4-Tolerance design: given certain threshold for risk factor, what are the maximum allowable variational ranges for τ_c and $|R_{\text{out}}|$?

Q5-Risk diagram: is it possible to construct a diagram with risk factors showing at arbitrary combination of τ_c and $|R_{\text{out}}|$, thus encompassing answers for all the previous questions?

Q6-Sensitivity analysis: if the statistical descriptions of the uncertain flame parameters are modified, then how would this affect the risk diagram derived from Q5?

Q1 sets the stage for robust design analysis. Here, risk factor $P_f(\%)$ describes the probability that a thermoacoustic mode is unstable, which can be expressed as the following [8]:

$$P_f(\%) = 100 \int_0^\infty \text{PDF}(\alpha) d\alpha \quad (4)$$

where α stands for the modal growth rate. The risk analysis performed in Q1 serves as the foundation for the subsequent robust design analysis.

Q2 tries to increase the robustness of the system design by introducing a control factor: τ_c . In practice, τ_c can be tuned by

modifying the distance between the swirler and the combustor dump plane [27]. By adjusting the constructive/destructive interferences between the flame response to axial velocity fluctuations and the response to swirl number fluctuations, we are aiming at making the growth rates of both modes vary only in the stable region, thus mitigating the risk.

Q3 goes one step further toward reality compared to Q2: τ_c can be easily influenced by the perturbations of the convective velocity in the swirler tube, and the reflection coefficient $|R_{out}|$, which largely depends on the turbine operating conditions, is inherently uncertain. By additional acknowledgment of the uncertainties in flame and acoustic boundary parameters, the robustness of the system can be further enhanced.

Q4 approaches the robust design via the perspective of an *inverse problem*: searching the maximum allowable variational ranges for the uncertain parameters while still satisfying the constraints. This is beneficial toward understanding, e.g., the trade-off between combustor and turbine operational uncertainties, thus achieving a better coordination between combustor and turbine design groups.

Q5 aims higher by proposing the concept of a risk diagram, which provides the distribution of risk factor over the entire the parameter space. This task extends Q1 to enable the practitioner to conveniently locate the desired parameter regions for achieving efficient optimum search performed in Q2, Q3, and Q4.

Finally, Q6 mimics the situation that our knowledge of the uncertain parameters, which is reflected in their assigned PDF, will be updated as the design process evolves. Therefore, it is necessary to reconduct the risk analysis and assess the sensitivity of results to different distribution types of parameters.

As progressing from Q1 to Q6, the dramatically increased problem complexity and associated computational cost prohibit a direct application of acoustic solvers, including the relatively cheap acoustic network model. However, surrogate modeling technique turns this around and opens new possibilities for addressing robust design problems efficiently, which we discuss in Sec. 4.

4 Gaussian Process Modeling

To efficiently address the robust design tasks outlined in Sec. 3.3, a machine learning method called GP is employed and corresponding solution strategies are constructed. In the context of thermoacoustic analysis, Schneider et al. [28] employed GP to construct a real-time modeling approach to simulate pressure pulsation amplitudes of an annular gas turbine combustor. The accuracy of their approach was further verified on the measured data for a wide range of operating conditions. In a recent work, Chattopadhyay et al. [29,30] adopted a GP model to predict combustor instability at untried operational conditions and successfully benchmarked the results with the experimental data. In the following, we first briefly review the fundamentals of GP modeling. Afterward, we train a total of four surrogate models for predicting modal frequencies and growth rates of the ITA and cavity modes, respectively, which will be repetitively used for addressing different robust design tasks in the subsequent sections. We close this section with a brief comparison of the GP approach with other UQ methods. The GP model training is performed via UQLab [31].

4.1 Fundamentals Overview. Gaussian process modeling is a supervised learning technique in machine learning domain [32]. Based on carefully selected training samples and their corresponding responses, GP is capable of training a computationally efficient surrogate model to approximate the original high-fidelity solver. As a result, the UQ analysis nested in the robust design procedure can be performed directly on the trained GP model; thus, repetitive high-fidelity solver calls can be avoided and the overall efficiency of the robust design analysis can be significantly improved. In the following, we summarize the key features of GP modeling. Jones et al. [33] provides a complete derivation of GP

method and Forrester and Keane [34] review the topic of employing GP in the context of surrogate modeling. For the application of GP modeling in robust design in other domains, we refer readers to Refs. [35] and [36].

GP modeling treats the output $f(\mathbf{x})$ of the high fidelity model at \mathbf{x} (a vector with the entries being the individual input parameter) as the realization of a Gaussian process

$$f(\mathbf{x}) = \beta + Z(\mathbf{x}) \quad (5)$$

where β is a constant value and $Z(\mathbf{x})$ corresponds to the departure from β at \mathbf{x} , which is modeled as a Gaussian stochastic function with zero mean, variance σ^2 , and covariance defined as

$$\text{Cov}[Z(\mathbf{x}^i, \mathbf{x}^j)] = \sigma^2 R(\mathbf{x}^i, \mathbf{x}^j) \quad (6)$$

where $R(\mathbf{x}^i, \mathbf{x}^j)$ is the correlation function between any two locations \mathbf{x}^i and \mathbf{x}^j in the input parameter space. In this study, a Gaussian correlation function is adopted to describe $R(\mathbf{x}^i, \mathbf{x}^j)$, which can be written as

$$R(\mathbf{x}^i, \mathbf{x}^j) = \exp \left[- \sum_{k=1}^M \theta_k (x_k^i - x_k^j)^2 \right] \quad (7)$$

where M denotes the dimension of the input (i.e., number of input parameters), subscript k represents the k th component of the input vector \mathbf{x} , and $\theta = [\theta_1, \dots, \theta_M]$ controls the level of correlation in the corresponding dimension: a high value of θ_i signifies a high rate of decay of correlation in the i th dimension, and vice versa.

Based on a set of training samples $\mathbf{X}_D = [\mathbf{x}^1, \dots, \mathbf{x}^N]^T$ and their corresponding responses $\mathbf{Y}_D = [f(\mathbf{x}^1), \dots, f(\mathbf{x}^N)]^T$, we can train the GP model by finding values for β , σ^2 , and θ such that the likelihood of achieving the observations (training samples and their corresponding responses) is maximized. For any given GP model parameter set $(\beta, \sigma^2, \theta)$, the likelihood function L can be directly obtained from the probability density function of a multivariate normal distribution

$$L(\beta, \sigma^2, \theta | \mathbf{X}_D, \mathbf{Y}_D) = \frac{1}{(2\pi\sigma^2)^{N/2} |\mathbf{R}|^{1/2}} \times \exp \left[- \frac{1}{2\sigma^2} (\mathbf{Y}_D - \beta \mathbf{1})^T \mathbf{R}^{-1} (\mathbf{Y}_D - \beta \mathbf{1}) \right] \quad (8)$$

where $\mathbf{1}$ is a vector of ones of dimension M . In practice, the logarithm of the above likelihood function is being maximized, which can be written as

$$\ln(L(\beta, \sigma^2, \theta | \mathbf{X}_D, \mathbf{Y}_D)) = - \frac{N}{2} \ln(2\pi) - \frac{N}{2} \ln(\sigma^2) - \frac{1}{2} \ln(|\mathbf{R}_D|) - \frac{1}{2\sigma^2} (\mathbf{Y}_D - \beta \mathbf{1})^T \mathbf{R}_D^{-1} (\mathbf{Y}_D - \beta \mathbf{1}) \quad (9)$$

By setting the derivatives of Eq. (9) with respect to β and σ^2 to zeros, we can obtain their maximum likelihood estimation

$$\hat{\beta} = (\mathbf{1}^T \mathbf{R}_D^{-1} \mathbf{1})^{-1} \mathbf{1}^T \mathbf{R}_D^{-1} \mathbf{Y}_D \quad (10)$$

$$\hat{\sigma}^2 = \frac{1}{N} (\mathbf{Y}_D - \hat{\beta} \mathbf{1})^T \mathbf{R}_D^{-1} (\mathbf{Y}_D - \hat{\beta} \mathbf{1}) \quad (11)$$

For estimating θ , the following auxiliary optimization problem has to be solved:

$$\hat{\theta} = \arg \max_{\theta} \left[- \frac{N}{2} \ln(\hat{\sigma}^2) - \frac{1}{2} \ln(|\mathbf{R}_D|) \right] \quad (12)$$

Finally, the GP model prediction $\hat{f}(\mathbf{x})$ at an arbitrary location \mathbf{x} is

$$\hat{f}(\mathbf{x}) = E[G(\mathbf{x})|X_D, Y_D] = \hat{\beta} + \mathbf{r}(\mathbf{x})^T \mathbf{R}_D^{-1} (Y_D - \mathbf{1}\beta) \quad (13)$$

which is interpreted as the conditional expectation of the Gaussian process $G(\mathbf{x})$, conditional on the known responses of the training samples [37]. $\mathbf{r}(\mathbf{x})$ in Eq. (13) is the correlation vector between \mathbf{x} and all the training samples, i.e., $\mathbf{r}(\mathbf{x}) = [\mathbf{R}(\mathbf{x}, \mathbf{x}^1), \dots, \mathbf{R}(\mathbf{x}, \mathbf{x}^N)]$.

At training sample locations $\mathbf{x}^1, \mathbf{x}^2, \dots, \mathbf{x}^N$, the following condition is fulfilled:

$$\hat{f}(\mathbf{x}^i) = f(\mathbf{x}^i) \quad (14)$$

indicating that GP surrogate modeling is an interpolation method that produces the exact responses at corresponding training sample locations.

4.2 Gaussian Process Model Training. In this study, we strive to train four separate, generally applicable GP models for approximating the frequency and growth rate of ITA and cavity modes, respectively, covering the whole parameter range specified in Table 1. The robust design analysis conducted in Sec. 5 will be configured completely upon the models trained in this section, i.e., no additional training will be needed.

Figure 5 summarizes the flowchart for training the GP models. The training (as well as the employment of GP models in Sec. 5) is performed on an Intel Core i5-6200U CPU 2.30GHz laptop PC. Details for each step are given in the following:

Step 1: We start the training process by uniformly drawing 18 samples of $(\tau_1, \sigma_1, \tau_c, \tau_{s1}, \tau_{s2}, |R_{out}|)$ from the parameter space specified in Table 1, via a Halton sequence [38], which is a low-discrepancy sampling method that possesses an excellent space-filling property. Loepky et al. [39] suggested that approximately a sample size of $10M$ (M is the number of input parameters) is required when using GP to approximate the target response. Therefore, we use a third of $10M$ (18 in this case) as our initial sample size. Subsequently, we can construct the design matrix X_D as Eq. (15), with each row representing one sample

$$X_D = \begin{bmatrix} \tau_1^{(1)} & \sigma_1^{(1)} & \tau_c^{(1)} & \tau_{s1}^{(1)} & \tau_{s2}^{(1)} & |R_{out}|^{(1)} \\ \tau_1^{(2)} & \sigma_1^{(2)} & \tau_c^{(2)} & \tau_{s1}^{(2)} & \tau_{s2}^{(2)} & |R_{out}|^{(2)} \\ \vdots & \vdots & \vdots & \vdots & \vdots & \vdots \\ \tau_1^{(18)} & \sigma_1^{(18)} & \tau_c^{(18)} & \tau_{s1}^{(18)} & \tau_{s2}^{(18)} & |R_{out}|^{(18)} \end{bmatrix} \quad (15)$$

Step 2: For each sample, we calculate the corresponding output quantities via acoustic network: ITA mode frequency ω^{ITA} , ITA mode growth rate α^{ITA} , cavity mode frequency ω^{CAV} , and cavity mode growth rate α^{CAV} . We store them in the response matrix $Y_D = [\omega^{ITA}, \alpha^{ITA}, \omega^{CAV}, \alpha^{CAV}]$, with each column vector containing the corresponding response values of all the samples in X_D .

Step 3: We train four separate GP models by using the following “sample-response” pairs: (X_D, ω^{ITA}) , (X_D, α^{ITA}) , (X_D, ω^{CAV}) and (X_D, α^{CAV}) .

Step 4: We perform leave-one-out cross-validation [31] to judge the prediction accuracy of all four GP models. Leave-one-out cross-validation estimates the generalization error (GE) of the GP model in the following manner:

$$GE = \frac{1}{N} \sum_{i=1}^N \left(f_i - \hat{f}_i^{(-i)} \right)^2 \quad (16)$$

where N denotes the total number of training samples, f_i corresponds to the known response of the training sample \mathbf{x}^i , and $\hat{f}_i^{(-i)}$

represents the prediction at \mathbf{x}^i using the GP model constructed upon all training samples except (\mathbf{x}^i, f_i) .

Step 5: If the prediction accuracy for any GP models is not satisfied, we draw six new samples from the Halton sequence and expand X_D , run the acoustic network solver to calculate the responses of these new samples, augment Y_D by the newly obtained responses, and start another round of model training and validating. We choose to update six samples at once to take advantage of parallel computing, which would be especially important when expensive solvers are employed.

Step 6: The process continues until the model generalization errors are saturated.

Figure 6 displays the convergence history of the generalization errors of all four GP models as training samples are enlarged iteratively. It can be seen that after 15 iterations, i.e., a total of 102 $(18 + 14 \times 6)$ training samples are employed, the generalization errors for frequency and growth rate predictions have saturated, thus implying that all four GP models have converged. The total training time is 93 s.

To further test the accuracy of the newly trained GP model, another 50 samples of $(\tau_1, \sigma_1, \tau_c, \tau_{s1}, \tau_{s2}, |R_{out}|)$ were randomly draw, which are not included in the training samples, and compare the GP-predicted responses with the true responses calculated via acoustic network at these sample locations. We emphasize that this is only for the purpose of verification, but not necessary for the GP model training.

The comparisons shown in Fig. 7 confirm the results given by the error diagnoses in Fig. 6. Therefore, we can see that with only a modest number of training samples, the obtained GP models have already achieved high predicting accuracy and applicable over a large parameter space.

4.3 Comparisons With Other Uncertainty Quantification Methods. In the context of accelerating the UQ analysis in thermoacoustic instability analysis, various methods have been proposed and validated on their corresponding problem settings: a polynomial-based regression method [9] and an analytical method [8], which enjoy simplicity but so far have only dealt with flame model uncertainties; Adjoint-based methods [10–12], which enjoy mathematical elegance and are free of the “curse of dimensionality,” but most effective for small parameter variational ranges and may miss the global optimum when combined with a gradient-based optimization routine; polynomial chaos expansion [14,15,40], which shows computational efficiency for a small number of uncertain parameters, but relies on the specific PDFs of the input parameters to determine the expansion and also works best on a rather small parameter variational ranges; *active*

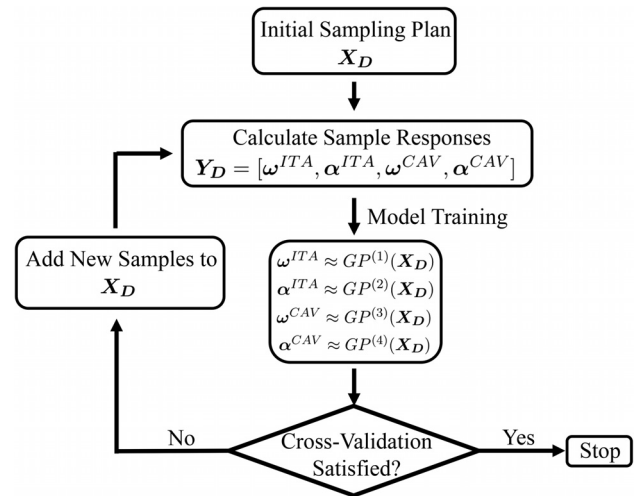


Fig. 5 Flowchart of GP model training

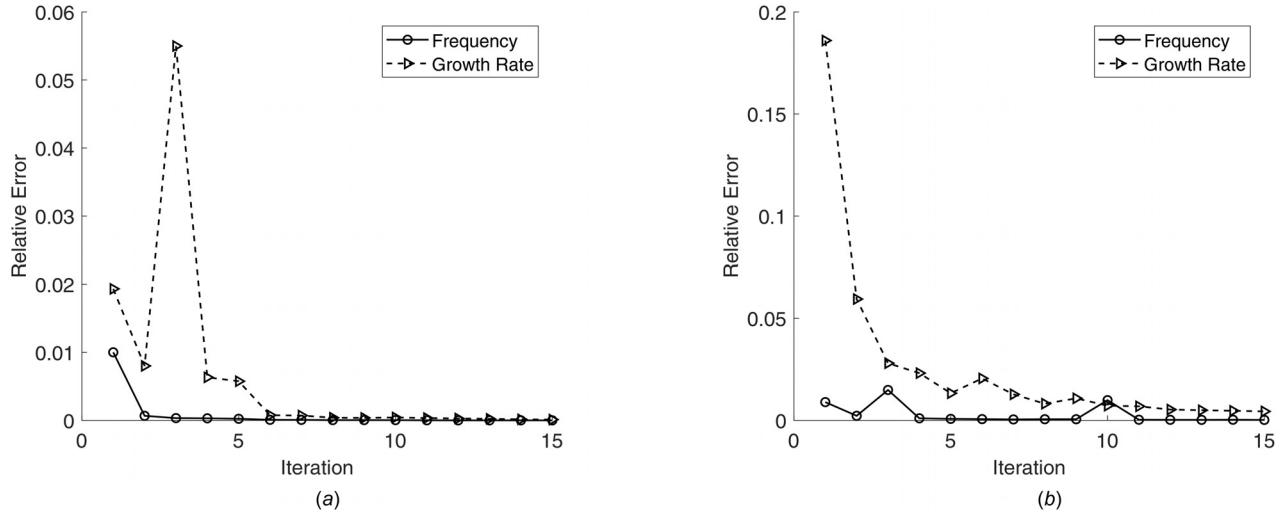


Fig. 6 Convergence history of the GP models for approximating (a) ITA and (b) cavity mode. For each GP model, the GE calculated via Eq. (16) is scaled by the variance of the responses of the training sample and shown as the relative error in the figure. For both modes, frequency converges faster than growth rate. The relative error of the ITA mode is smaller than the cavity mode.

subspace approach [8,13], which leverages on the low-dimensional subspace of the original system to accelerate the analysis, but the existence of this low-dimensional subspace is not guaranteed for general problems.

Gaussian process approach, on the other hand, fits perfectly in the context of robust design, with its capability of handling large parameter variational ranges and various probability distribution types, provided that the number of the input parameters is moderate (smaller than 20 [41]). We will demonstrate its accuracy and efficiency in Sec. 5.

5 Robust Design Analysis

In this section, we exploit the GP models trained from the last section to address the proposed robust design problems outlined in Sec. 3.3. Each subsection is devoted to one problem, starting with the problem statement, followed by the solution strategy, results, demonstration, and validation.

5.1 Risk Analysis

“Q1: what is the risk factor of the system when uncertainties are presented in the flame parameter τ_1 , σ_1 , τ_{s1} , and τ_{s2} ?”

Here, we consider τ_c and $|R_{out}|$ to be fixed at their nominal values, while τ_1 , σ_1 , τ_{s1} , τ_{s2} follow independent uniform distributions with the parameter range indicated in Table 1. When flame parameters are uncertain, the growth rate values for both modes will also exhibit variation, thus having the potential to be unstable. Therefore, this is a typical *forward uncertainty quantification* [8] problem.

To calculate the risk factor, we can approximate Eq. (4) via Monte Carlo simulation [13] by repeatedly calculating the growth rates of different samples of $(\tau_1, \sigma_1, \tau_{s1}, \tau_{s2})$ and then compute the ratio between the number of samples with growth rate larger than zero and the total number of samples. Instead of calculating the growth rate with the acoustic solver, which might be computationally very expensive, we perform Monte Carlo directly on the GP models, thus significantly accelerating the analysis due to its negligible predicting cost. We randomly draw 20,000 samples of $(\tau_1, \sigma_1, \tau_{s1}, \tau_{s2})$ from their distributions for Monte Carlo simulation, which are large enough to ensure the statistical convergence of the obtained PDFs.

Probability density functions of growth rate and frequency of both ITA mode and cavity mode are shown in Fig. 8. The diagonal figures display the marginal distributions while the off-diagonal figure shows their joint distribution. Comparisons against the reference PDFs, which are obtained via applying the Monte Carlo directly on the acoustic network solver using the same 20,000 samples, are also made and shown in Fig. 8. R^2 coefficient (defined in Appendix C) is employed to quantify the accuracy of the GP approximation. Excellent matches between GP models and full thermoacoustic model for both modes are observed, thus demonstrating the high predictive accuracy of the trained GP models. In terms of computation time, the full Monte Carlo simulation performed via acoustic network solver takes 271 s, while GP models only require 1.3 s. We emphasize that this acceleration of UQ analysis will be even more significant when GP method is adopted to approximate other more sophisticated thermoacoustic models, and when a complete robust design task is required where multiple times of UQ analyses have to be performed.

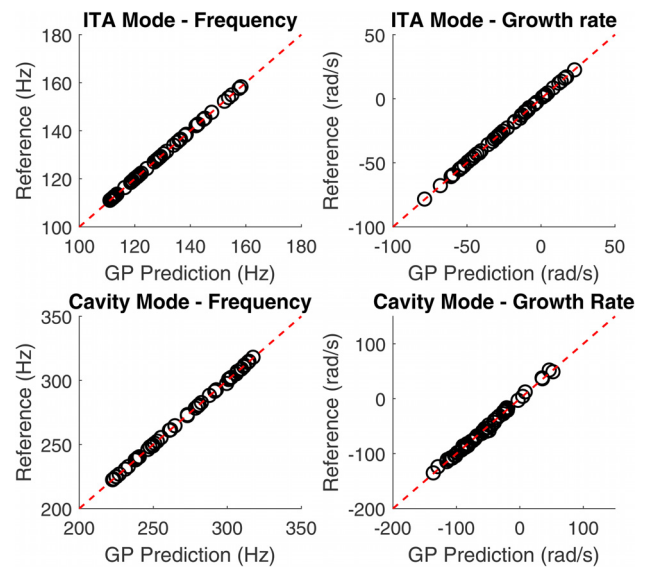


Fig. 7 Comparisons between GP model predictions and the reference values produced by acoustic network solver

5.2 Ideal Control Design

“Q2: using τ_c as a control factor, what is the required minimum modification of τ_c to eliminate the risk of instability of both cavity and ITA mode simultaneously?”

As in Sec. 5.1, we consider independent uniform distributions with variational ranges specified in Table 1 for τ_1 , σ_1 , τ_{s1} , τ_{s2}

and assume that the exit reflection coefficient $|R_{out}|$ is fixed at its nominal value. We try to optimize the time lag τ_c of swirl fluctuations under the constraint that the risk factors of both modes ($P_f^{(I)}$ for the ITA mode and $P_f^{(C)}$ for the cavity mode) are small. This optimization problem is explicitly expressed as follows:

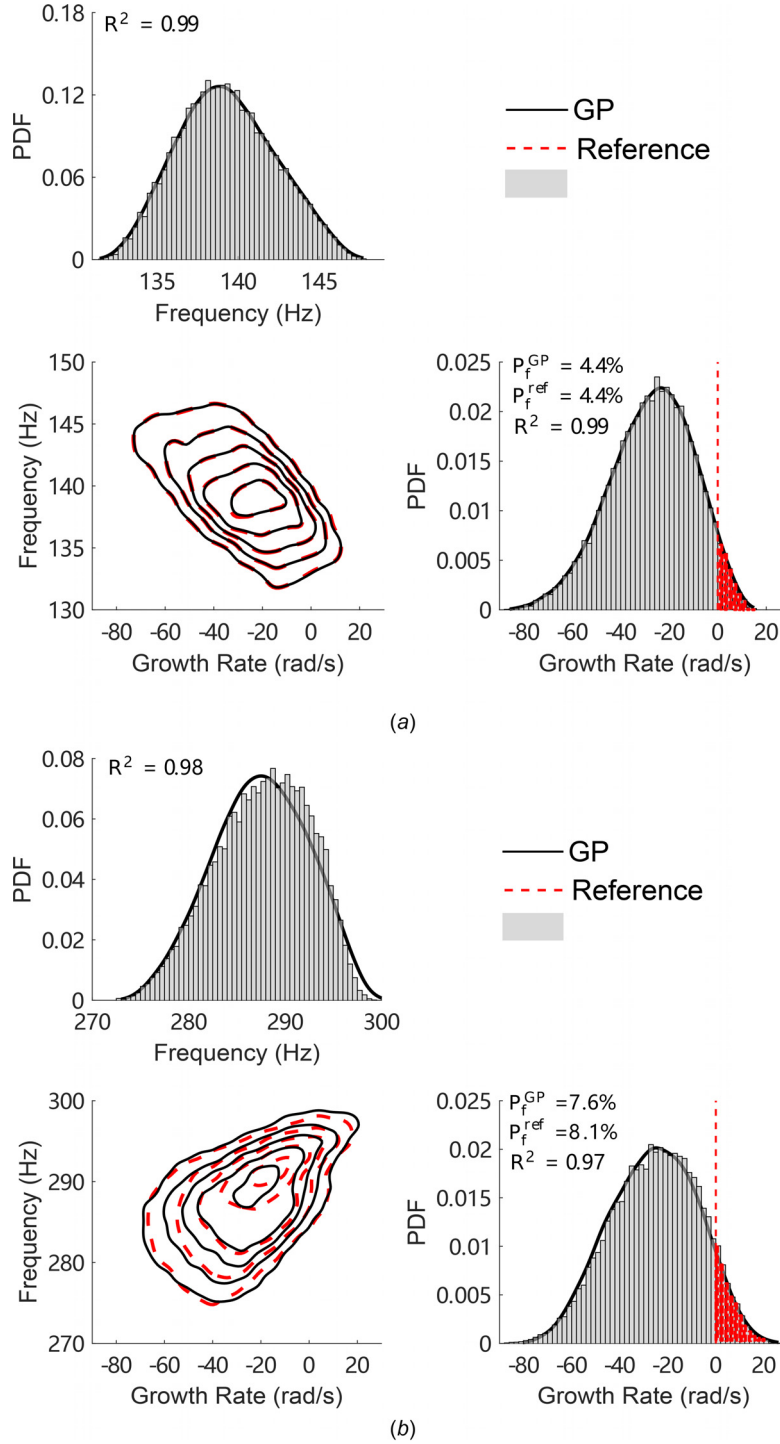


Fig. 8 PDFs of the modal frequency and growth rate given by the GP models and reference acoustic solver are compared. Diagonal figures are marginal distributions while off-diagonal figure is the joint distribution. Same Monte Carlo samples are used for both GP models and acoustic network solver: (a) ITA mode and (b) cavity mode.

$$\begin{aligned}
& \min_{\tau_c} f(\tau_c) = (\tau_c - \tau_c^0)^2 \\
& \text{subject to: } P_f^{(I)}(\tau_c) \leq 0.1\% \\
& \quad P_f^{(C)}(\tau_c) \leq 0.1\% \\
& \quad 0.66\tau_c^0 \leq \tau_c \leq 1.6\tau_c^0
\end{aligned} \tag{17}$$

The first line represents the objective of the optimization, i.e., that the modification of τ_c from its nominal value τ_c^0 is minimum.

Notice that the goal of mitigating instability risk is formulated as constraints on $P_f^{(I)}$ and $P_f^{(C)}$ instead of as objectives. The optimal value of τ_c should lie within the range in Table 1. This condition is also expressed as a constraint. The formulation (17) of the optimization problem Q2 assures its well posedness, since the minimum possible value of P_f is zero and there may exist multiple τ_c 's that lead to zero P_f . Thus, we seek the *minimum* modification of τ_c from τ_c^0 that satisfies the constraint of zero instability risk, thus ensuring that only a single optimum exists.

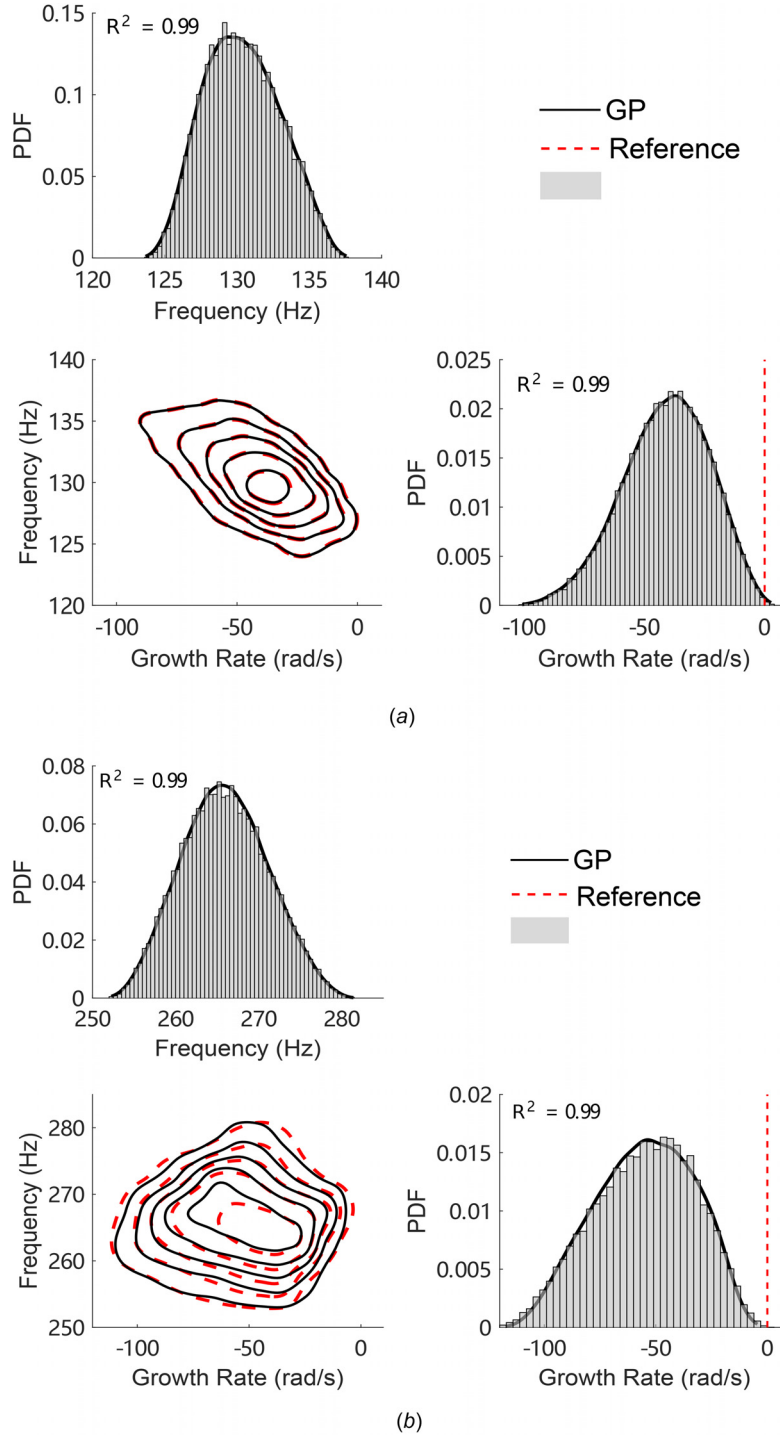


Fig. 9 PDFs of the modal frequency and growth rate predicted by the GP models and reference acoustic solver are compared. Indeed, with $\tau_c = \tau_c^{\text{opt}}$, the instability risks of both modes are basically eliminated: (a) ITA mode and (b): cavity mode.

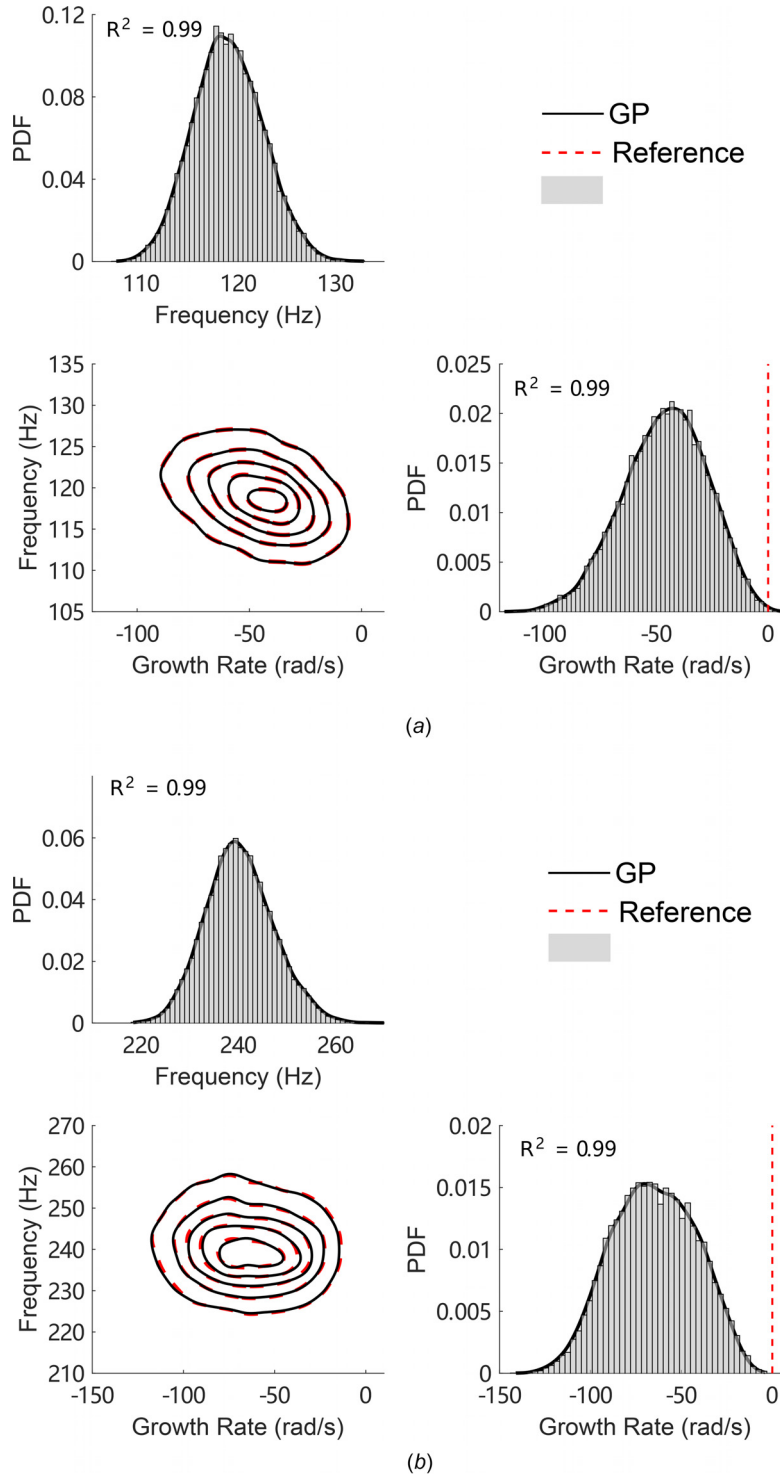


Fig. 10 PDFs of the modal frequency and growth rate predicted by the GP models and reference acoustic solver are compared. Here, $\tau_c \sim \mathcal{N}(\tau_c^{\text{opt}}, (0.05\tau_c^{\text{opt}})^2)$, $|R_{\text{out}}| \sim \mathcal{U}(0.7, 0.9)$ and $\tau_1, \sigma_1, \tau_{s1}, \tau_{s2}$ follow independent uniform distribution with variational ranges specified in Table 1: (a) ITA mode and (b) cavity mode.

Since $P_f^{(l)}$ and $P_f^{(c)}$ are both nonlinear functions of τ_c , Eq. (17) constitutes a single-variable, nonlinear constrained global optimization problem. Therefore, we employ a *pattern search* algorithm [42] to optimize τ_c . For each optimization iteration, $P_f^{(l)}$ and $P_f^{(c)}$ are computed by the same way as presented in Q1. Since a global optimization search usually involves more than a handful of iterations, using efficient GP models to repeatedly calculate P_f within each iteration could potentially achieve a significant reduction of

computational cost. It is worth mentioning that other more advanced global optimization algorithms can also be employed here. A thorough comparison between different optimization routines is beyond the scope of this paper.

The global optimum result identified by the pattern search algorithm is $\tau_c^{\text{opt}} = 3.52$ ms. To verify this result, we perform a Monte Carlo simulation as in Q1 by setting $\tau_c = \tau_c^{\text{opt}}$. Twenty thousand samples of $(\tau_1, \sigma_1, \tau_{s1}, \tau_{s2})$ are employed to ensure statistical

convergence. PDFs of frequency and growth rate for both modes are shown in Fig. 9, where the reference PDFs obtained by applying Monte Carlo directly on acoustic solver are also shown. It can be seen that, with this value of τ_c , P_f for both modes are basically zero, and the PDFs predicted by GP models match very well with the reference results.

5.3 Realistic Control Design

“Q3: in reality, we cannot perfectly control τ_c . Meanwhile, $|R_{out}|$ is also uncertain. Then how would these affect the decision made from Q2?”

As in Sec. 5.1, we consider τ_1 , σ_1 , τ_{s1} , and τ_{s2} to follow independent uniform distribution with variational ranges specified in Table 1. Now, we consider $|R_{out}|$ to be uncertain, following a uniform distribution in the range 0.7–0.9. For τ_c , a Gaussian distribution is assigned with mean $\bar{\tau}_c$ and standard deviation 5% of τ_c^0 . Here, the standard deviation is used to mimic the situation that τ_c cannot be perfectly predicted, and statistically exhibits fluctuation around its design value $\bar{\tau}_c$. We aim to optimize $\bar{\tau}_c$ with the constraints being P_f of both modes are sufficiently small, and objective function being the modification of $\bar{\tau}_c$ from its nominal value is minimum. We can explicitly express this optimization problem as follows:

$$\begin{aligned} \min_{\bar{\tau}_c} f(\bar{\tau}_c) &= (\bar{\tau}_c - \tau_c^0)^2 \\ \text{subject to: } P_f^{(l)}(\tau_c) &\leq 0.1\% \\ P_f^{(c)}(\tau_c) &\leq 0.1\% \\ \tau_c &\sim \mathcal{N}(\bar{\tau}_c, (0.05\tau_c^0)^2) \end{aligned} \quad (18)$$

The global optimum result is $\bar{\tau}_c^{\text{opt}} = 4.06$ ms, which is obtained via the same optimization algorithm employed in Sec. 5.2. To verify this result, we perform a Monte Carlo simulation by setting $\tau_c \sim \mathcal{N}(\bar{\tau}_c^{\text{opt}}, (0.05\tau_c^0)^2)$, $|R_{out}| \sim \mathcal{U}(0.7, 0.9)$ and τ_1 , σ_1 , τ_{s1} , τ_{s2} follow independent uniform distribution with variational ranges specified in Table 1. Twenty thousand samples of $(\tau_1, \sigma_1, \tau_c, \tau_{s1}, \tau_{s2}, |R_{out}|)$ are used to ensure statistical convergence. PDFs of both frequency and growth rates of both modes are shown in Fig. 10, where the reference PDFs given by applying Monte Carlo directly on acoustic solver are also shown.

It can be seen that the PDFs predicted by GP models match very well with the reference results. Also, we notice that when taking into account the uncertainties in $|R_{out}|$ and imperfect control of τ_c , the optimum decision made from Q2 is not valid anymore. Instead, the design value for τ_c should increase from τ_c^{opt} to $\bar{\tau}_c^{\text{opt}}$ to eliminate the instability risk for both modes, as indicated in Fig. 10. Here, we emphasize that although we take into account more sources of uncertainties with mixed distribution type compared to Q2, our GP models manage to capture the induced variations of both eigenmodes, thus showing a high level of both flexibility and accuracy.

5.4 Tolerance Design

“Q4: given a certain threshold for risk factor, what are the maximum allowable variational ranges for τ_c and $|R_{out}|$?”

Here, we aim to investigate the compromise between the allowable uncertainty level of τ_c and $|R_{out}|$, based on the optimum result obtained from Q3. To be more specific, by considering $\tau_c \sim \mathcal{N}(\bar{\tau}_c^{\text{opt}}, (\sigma_{\tau_c})^2)$ and $|R_{out}| \sim \mathcal{U}(R_L, 0.9)$, we seek the trade-off between σ_{τ_c} (standard deviation of τ_c) and R_L (lower bound of $|R_{out}|$), both of which serve as the indications of the corresponding parameter allowable uncertainty level. For τ_1 , σ_1 , τ_{s1} , and τ_{s2} , we consider them to follow independent uniform distribution with variational ranges specified in Table 1. We formulate Q4 as a multi-objective optimization problem, which can be explicitly expressed as

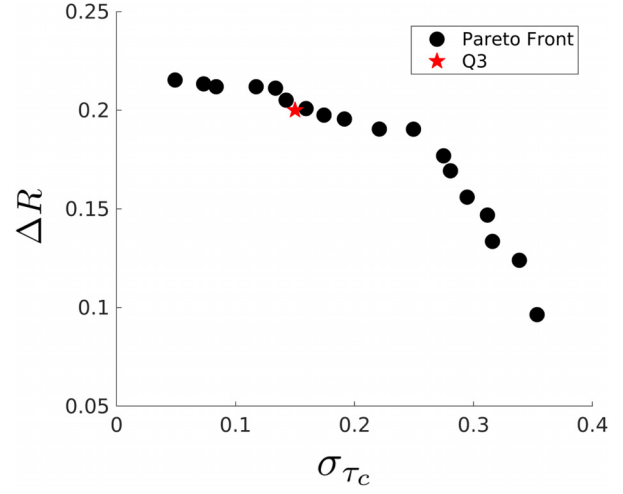


Fig. 11 Pareto front of the two objectives: maximize σ_{τ_c} and maximize the variational range for $|R_{out}|$. The y-axis $\Delta R = |R_{out}|^0 - R_L$. Red star marks the optimum result of Q3, from which we can see its relative location on the overall Pareto front.

$$\begin{aligned} \max_{\sigma_{\tau_c}} f(\sigma_{\tau_c}) &= \frac{\sigma_{\tau_c}}{\tau_c^0} \\ \min_{R_L} g(R_L) &= \frac{R_L}{|R_{out}|^0} \\ \text{subject to: } P_f^{(l)}(\tau_c, |R_{out}|) &\leq 0.1\% \\ P_f^{(c)}(\tau_c, |R_{out}|) &\leq 0.1\% \\ \tau_c &\sim \mathcal{N}(\bar{\tau}_c, (\sigma_{\tau_c})^2) \\ |R_{out}| &\sim \mathcal{U}(R_L, 0.9) \end{aligned} \quad (19)$$

Notice that we are dealing with two variables, two objective functions, and $P_f^{(l)}$ and $P_f^{(c)}$ are both nonlinear functions of τ_c and $|R_{out}|$. Therefore, Eq. (19) constitutes a multivariable, multi-objective, nonlinear constrained global optimization problem. For multi-objective optimization problems, it is usually the case that not all the objectives can be optimized simultaneously. Indeed, there must be a trade-off in some way. Therefore, it would be more informative to introduce the concept of a *noninferior* solution, i.e., a solution where neither objective can be improved without degrading the other objectives. By locating a set of these noninferior solutions in the objective space, which is also called *Pareto front* [43], we can visualize the trade-offs between different objectives conveniently.

Toward that end, we employ the *multi-objective pattern search* algorithm [44] to locate the Pareto front of the two objectives. $P_f^{(l)}$ and $P_f^{(c)}$ are efficiently calculated via the same way presented in Q1.

The results are shown in Fig. 11, where the optimum result obtained from Q3 is also displayed. It can be seen that two objectives are competing with each other: toward the right of the Pareto front, a larger σ_{τ_c} would require smaller ΔR ; toward the left of the Pareto front, a smaller σ_{τ_c} would allow larger variational range for $|R_{out}|$. The qualitatively described trade-offs are beneficial to understand the interaction of the allowable uncertainty level between τ_c and $|R_{out}|$.

5.5 Risk Diagram

“Q5: is it possible to construct a diagram with risk factors shown at arbitrary combinations of τ_c and $|R_{out}|$, thus encompassing answers for all the previous questions?”

Here, we aim to compute the P_f 's for both modes at arbitrary location in the parameter space of τ_c and $|R_{out}|$, and illustrate them in a single risk diagram. As in Sec. 5.1, we consider τ_1 , σ_1 , τ_{s1} , τ_{s2} to

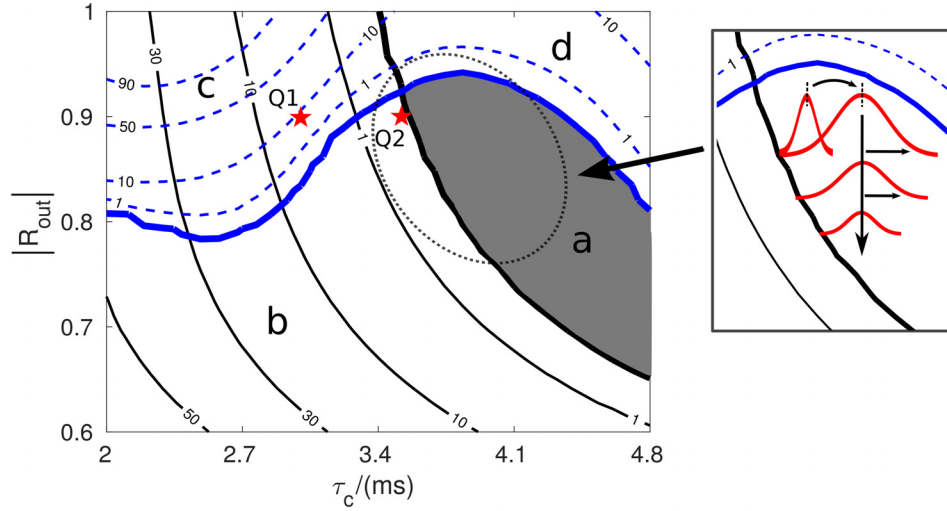


Fig. 12 Risk factor contours for both modes (blue for cavity mode and black for ITA mode). Zero risk lines (thick lines) divide the whole parameter space into four regions, with region a (shaded in grey) being the risk-free region. Results for Q1 and Q2 can be directly obtained from the diagram. For Q3 and Q4, the risk diagram offers a convenient visualization of the trade-off between τ_c 's mean location, τ_c 's uncertainty level and $|r_{out}|$'s uncertainty level. (For color figure please refer to online version.)

follow independent uniform distribution with variational ranges specified in Table 1.

To obtain such a risk diagram, we conduct a full factorial design [45] with a 30×30 uniformly spaced grid spanned over the parameter space of τ_c and $|R_{out}|$ (ranges indicated in Table 1), and we calculate the P_f 's for both modes at each combination of $(\tau_c, |R_{out}|)$ using the same method as presented in Q1. The potential excessive computational cost induced by this repetitive task is efficiently mitigated with GP models.

The risk diagram is depicted in Fig. 12, where risk factor contours for both ITA mode (black) and cavity mode (blue) are displayed. The thick lines mark the zero risk factor contour and they divide the parameter space of $(\tau_c, |R_{out}|)$ into four regions: region a is the risk-free region, i.e., when $(\tau_c, |R_{out}|)$ values are within this region, there is no risk for both modes to be unstable even though $\tau_1, \sigma_1, \tau_{s1}, \tau_{s2}$ are uncertain. Region b is dominated by the ITA mode, i.e., in this parameter region, cavity mode is stable while ITA mode exhibits instability risk. In region c, both modes have a certain level of risk to be unstable. Finally, region d is dominated by the cavity mode, i.e., in this parameter region, ITA mode is stable while cavity mode exhibits instability risk.

For the BRS burner investigated in this current study, ITA mode and cavity mode response differently to the change of $|R_{out}|$, as observed and thoroughly discussed in Refs. [25] and [46]. This phenomenon is also reflected in the obtained risk diagram (Fig. 12): For the cavity mode, above the threshold (zero risk line), an increase of $|R_{out}|$ promotes instability risk; contrarily, for the ITA mode, increasing $|R_{out}|$ tends to reduce the instability risk. However, we caution the reader that care must be exercised when interpreting physics from Fig. 12: risk diagram is not a modal stability map, and zero risk factor lines presented here are not zero growth rate lines. Each location in the risk diagram is associated with a PDF of the modal growth rate, and the risk factor value at that location is determined by not only the mean but also the standard deviation as well as the skewness of that PDF.

This risk diagram also indicates all the results obtained from Q1 to Q4: For Q1, we can directly read the risk factor values for both modes based on the $(\tau_c, |R_{out}|)$ location on the diagram; For Q2, we can conveniently locate the τ_c^{opt} to mitigate instability risk while minimizing the modification of τ_c . For Q3 and Q4, we cannot directly obtain the answers due to the uncertainties exhibited in both τ_c and $|R_{out}|$. Nevertheless, the risk diagram shows the trade-off between $\bar{\tau}_c$, σ_{τ_c} and $\Delta|R_{out}|$: larger $\bar{\tau}_c$ accommodates

larger uncertainty of τ_c and $|R_{out}|$; For fixed $\bar{\tau}_c$, larger $\Delta|R_{out}|$ requires smaller σ_{τ_c} , while smaller $\Delta|R_{out}|$ allows larger σ_{τ_c} . Such information can guide detailed optimization analysis.

5.6 Sensitivity Analysis

"Q6: if the statistical descriptions of the uncertain flame parameters are modified, how would this affect the risk diagram derived from Q5"

Up till now, we have only considered $\tau_1, \sigma_1, \tau_{s1}, \tau_{s2}$ following independent uniform distribution. In Q6, we relieve this assumption and assess the sensitivity of the zero risk lines against the statistical descriptions of the uncertain flame parameters $\tau_1, \sigma_1, \tau_{s1}, \tau_{s2}$. Toward this end, we examine two other distributions for $\tau_1, \sigma_1, \tau_{s1}, \tau_{s2}$, i.e., uncorrelated and correlated Gaussian. Distribution parameters for different cases are summarized in Table 2. Here, we label case A as the uniform distribution case, case B as the uncorrelated Gaussian case, and case C as the correlated Gaussian case, where the mean $\mathbf{M} = (\tau_1^0, \sigma_1^0, \tau_{s1}^0, \tau_{s2}^0)$ and the covariance matrix \mathbf{C} are determined via a bootstrap analysis of surrogate time series of velocity fluctuations and flame heat release rate fluctuations. Details are given in Appendix A.

Figure 13 demonstrates the zero risk factor lines for cases A, B, and C. "Star" location is chosen for accuracy benchmark of the GP models (details in Appendix B). For Gaussian distribution cases B and C, $P_f \leq 0.1\%$ is considered as zero risk since the probability of instability is statistically sufficiently small that it basically would never happen in reality. Arrows indicate the evolution of zero risk factor lines from case A to case C. It can be seen that the distribution type of flame parameters has a significant impact on the risk diagram: compare case A with case B, when distribution type changes from uniform to Gaussian, zero risk factor lines for both modes move outward, thus expanding the

Table 2 Summary of different distributions under investigation

| Parameters | Case A | Case B | Case C |
|-------------|-----------------------------------------------|-------------------------------------------------|---------------------------------------|
| τ_1 | $\mathcal{U}(0.9\tau_1^0, 1.1\tau_1^0)$ | $\mathcal{N}(\tau_1^0, (0.03\tau_1^0)^2)$ | $\mathcal{N}(\mathbf{M}, \mathbf{C})$ |
| σ_1 | $\mathcal{U}(0.9\sigma_1^0, 1.1\sigma_1^0)$ | $\mathcal{N}(\sigma_1^0, (0.03\sigma_1^0)^2)$ | |
| τ_{s1} | $\mathcal{U}(0.9\tau_{s1}^0, 1.1\tau_{s1}^0)$ | $\mathcal{N}(\tau_{s1}^0, (0.03\tau_{s1}^0)^2)$ | |
| τ_{s2} | $\mathcal{U}(0.9\tau_{s2}^0, 1.1\tau_{s2}^0)$ | $\mathcal{N}(\tau_{s2}^0, (0.03\tau_{s2}^0)^2)$ | |

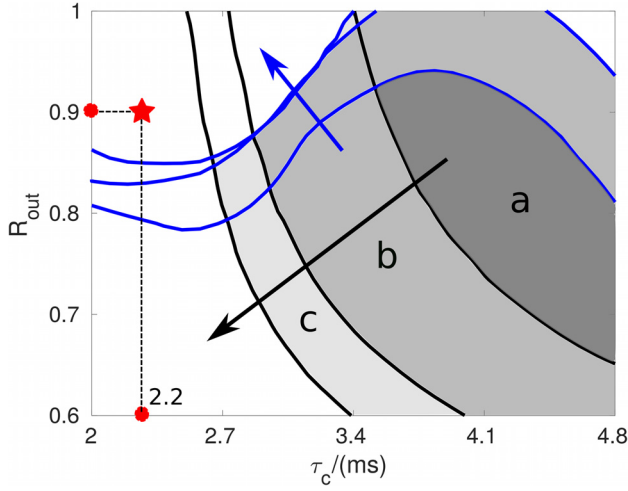


Fig. 13 Zero risk factor lines for cases a, b, and c, where blue and black lines correspond to the cavity mode and ITA mode, respectively. Risk-free zone keeps expanding from “a” (case a, uniform) to “a + b” (case b, uncorrelated Gaussian) and “a + b + c” (case c, correlated Gaussian). “star” location is chosen for accuracy benchmark of the GP models (details in Appendix B).

risk-free region to “a + b”; compare case B with case C, taking into account the correlations between the flame parameters results in further changes for cavity and ITA mode, thus gaining another risk-free region “c.” This expansion of risk-free zone from case A to C is due to the fact that a Gaussian distribution requires more samples to appear near the mean compared to an uniform distribution, and a correlated Gaussian further constrains the variational possibility of the parameters compared to an uncorrelated Gaussian. It is also interesting to see that the zero risk line of the ITA mode is more sensitive to the distribution type of the uncertain flame parameters, when comparing case B with C. However, this statement may not be generalized. Risk factor is a joint effect of the mean, standard deviation, and skewness of the PDF of the modal growth rate, all of which will be simultaneously influenced by the uncertainties of the flame parameters.

6 Conclusions

In this study, we systematically explored different scenarios in thermoacoustic robust design, ranging from basic risk analysis to control design and inverse tolerance design. In addition, we provided mathematical formulation and proposed efficient solution strategy for each of these problems. We introduced the concept of a risk diagram, which displays the risk factor values of multiple thermoacoustic modes at different locations in the parameter space under investigation, and we also assessed its sensitivity to the statistical descriptions of the underlying uncertain parameters.

Throughout this work, the Gaussian process modeling technique was employed, which trains a computationally efficient yet highly accurate surrogate model to approximate the thermoacoustic solver, thus efficiently mitigating the high computational cost induced by the forward uncertainty quantification embedded in the robust design analysis. The solutions for all the robust design tasks pursued in this work are based on one-time trained GP models. Considering the number, large variational ranges and mixed distribution types of the investigated uncertain parameters, GP models managed to deliver highly accurate results for multifaceted robust design tasks. We emphasize that the flexibility and efficiency offered by the GP approach would be more prominent when combined with more sophisticated and more comprehensive thermoacoustic solvers (e.g., Helmholtz solver, Linearized Navier–Stokes solver), leveraging on the better modeling capability they offer.

Future studies will focus on the following three aspects: (1) since GP modeling is a sampling-based approach, a limited number of training samples may introduce prediction uncertainties in the GP

model. Therefore, it is necessary to treat the parametric uncertainties and the surrogate modeling uncertainty concurrently in robust thermoacoustic design; (2) GP models also yield highly accurate approximations for modal frequency variations, thus opening new possibilities to include modal frequency as another constraint in robust thermoacoustic design; (3) we will employ GP method to approximate other more sophisticated thermoacoustic models, e.g., Helmholtz solver or linearized Navier–Stokes solver. Our preliminary work of extending GP to Helmholtz solver showed promising results, which will be demonstrated in the forthcoming papers. All the source code and data to reproduce the results presented in the current paper can be found online.²

Funding Data

- Chinese Scholarship Council (Grant No. 201606830045).

Nomenclature

- FIR = flame impulse response
- FTF = flame transfer function
- GP = Gaussian process
- h_i = FIR model coefficient
- ITA = intrinsic thermoacoustic mode
- N = number of FIR model coefficients
- PDF = probability density function
- P_f = risk factor (%)
- UQ = uncertainty quantification
- α = thermoacoustic modal growth rate
- σ_1 = standard deviation of the distributed time lags of flame response for axial velocity perturbation
- τ_c = time lag for swirl fluctuation traveling from swirler to flame base
- τ_{s1} = mean of the distributed time lags of flame response for swirl fluctuation (+)
- τ_{s2} = mean of the distributed time lags of flame response for swirl fluctuation (–)
- τ_1 = mean of the distributed time lags of flame response for axial velocity perturbation
- ω = thermoacoustic modal frequency
- $|R_{out}|$ = magnitude of reflection coefficients at combustor outlet

Appendix A: Determination of Covariance Matrix

We adopt the following procedure to determine the covariance matrix \mathbf{C} for case C in Q6:

- (1) Configure the reference FIR model using $(\tau_1^0, \sigma_1^0, \tau_{s1}^0, \tau_{s2}^0, \tau_c^0)$ via Eq. (1), use the time series of velocity perturbations (\mathbf{u}'_{ref}) from Ref. [8] (Fig. 1) as the reference input signal, compute the corresponding time series of heat release rate fluctuations (\mathbf{Q}'_{ref}) via the following equation:

$$\mathbf{Q}'_{ref,n} = \sum_{k=1}^L h_k \mathbf{u}'_{n-k} \quad (\text{A1})$$

- (2) Bootstrap analysis: For $i = 1, 2, \dots, 1000$, perform
 - (a) Generate a random white noise vector \mathbf{Q}'_e from $\mathcal{N}(0, \sigma_e^2)$ so that the signal-to-noise ratio is 5 (i.e., $\sigma_{\mathbf{Q}'_{ref}} / \sigma_e^2 = 5$).
 - (b) Let $\mathbf{Q}' = \mathbf{Q}'_e + \mathbf{Q}'_{ref}$, fix $\tau_c = \tau_c^0$, optimize $(\tau_1, \sigma_1, \tau_{s1}, \tau_{s2})$ so that the corresponding FIR model can produce \mathbf{Q}'_{FIR} which minimize $\|\mathbf{Q}'_{FIR} - \mathbf{Q}'\|_2$ given \mathbf{u}'_{ref} .
 - (c) Store the optimized results as $\mathbf{X}(i, :) = (\tau_1, \sigma_1, \tau_{s1}, \tau_{s2})^{(i)}$
- (3) (Calculate the 4-by-4 covariance matrix $\mathbf{C} = [C_{jk}]$ as

$$C_{jk} = \frac{1}{1000 - 1} \sum_{i=1}^{1000} (x_{ij} - \bar{x}_j)(x_{ik} - \bar{x}_k) \quad (\text{A2})$$

²<https://github.com/ShuaiGuo16/ASME19>

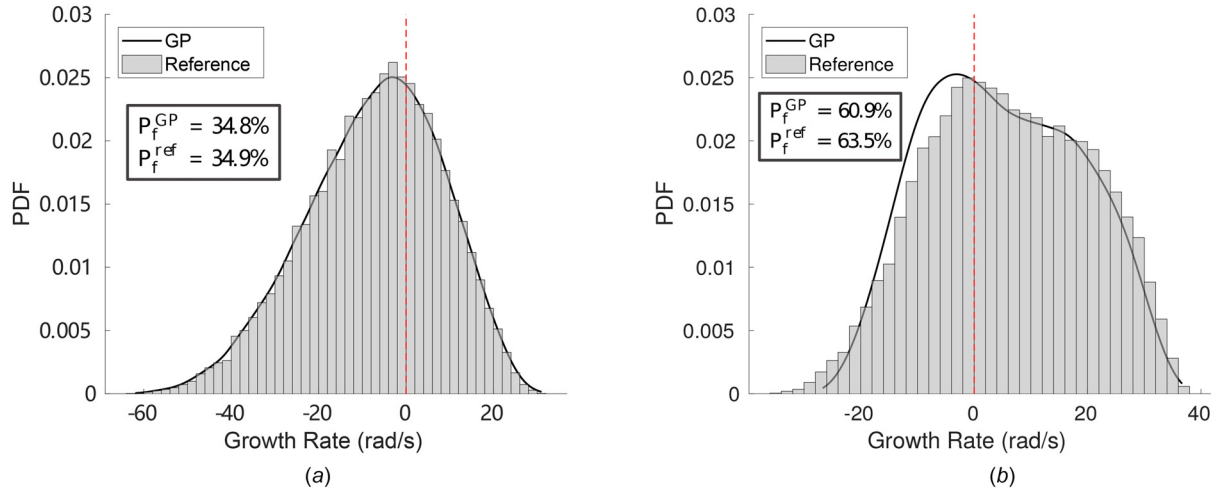


Fig. 14 PDF comparison: case A. (a) ITA mode and (b) cavity mode.

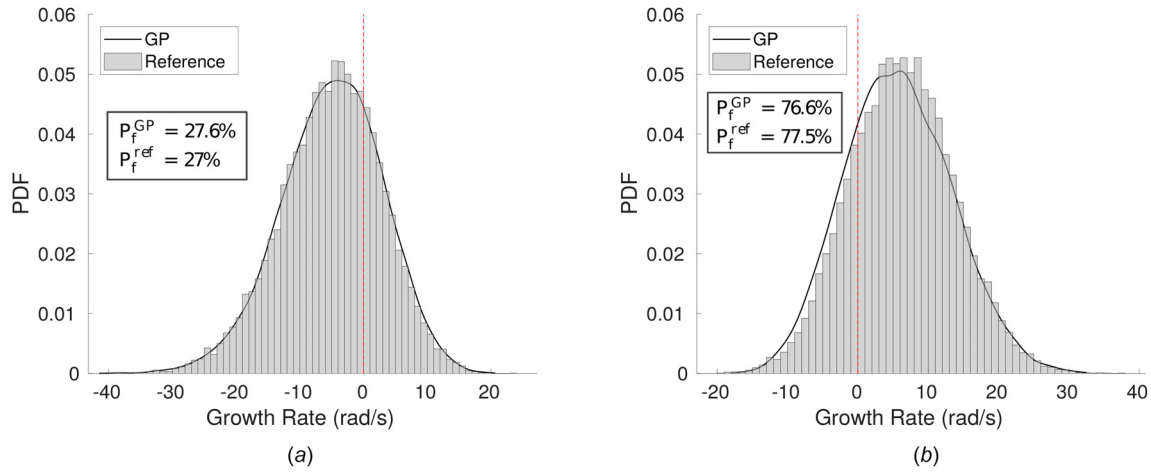


Fig. 15 PDF comparison: case B. (a) ITA mode and (b) cavity mode.

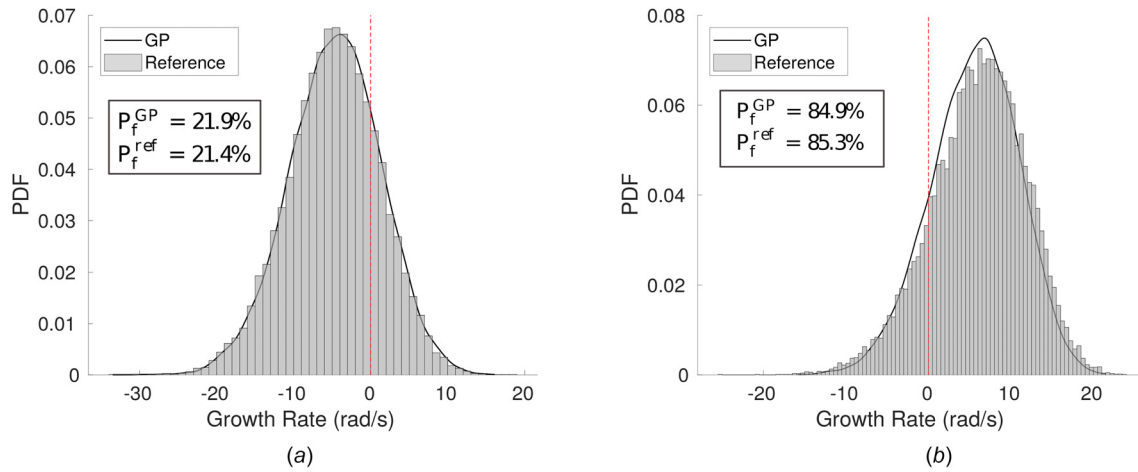


Fig. 16 PDF comparison: case C. (a) ITA mode and (b) cavity mode.

Appendix B: Accuracy Demonstrations of GP Models

We compare the PDFs of the modal growth rate predicted by the GP models and the acoustic solver. We choose $(\tau_c, |R_{out}|)$ to be the “star” location marked in

Fig. 13. The results for three different cases are shown in Figs. 14–16, respectively. For each case, we employ 20,000 samples in Monte Carlo simulation to obtain the converged results.

Appendix C: R^2 Coefficient

We adopt R^2 coefficient in Figs. 8–10 to quantitatively assess the accuracy of GP models in approximating eigenmodes (frequency and growth rate). R^2 coefficient is defined as

$$R^2 = 1 - \frac{\sum_{i=1}^N (X_i - Y_i)^2}{\sum_{i=1}^N (Y_i - \bar{Y})^2} \quad (C1)$$

where X and Y denote the quantity computed by GP models and acoustic network solver, respectively. \bar{Y} represents the mean value of the acoustic network solver predictions, and N represents the total number of Monte Carlo samples.

References

- [1] Lieuwen, T., and Yang, V., eds., 2005, *Combustion Instabilities in Gas Turbine Engines: Operational Experience, Fundamental Mechanisms, and Modeling* (Progress in Astronautics and Aeronautics, Vol. 210), AIAA, Reston, VA.
- [2] Juniper, M. P., and Sujith, R. I., 2018, "Sensitivity and Nonlinearity of Thermoacoustic Oscillations," *Annu. Rev. Fluid Mech.*, **50**(1), pp. 661–689.
- [3] Park, G. J., Lee, T. H., Lee, K. H., and Hwang, K. H., 2006, "Robust Design: An Overview," *AIAA J.*, **44**(1), pp. 181–191.
- [4] Ling, Y., Ryan, K., Asher, I., Kristensen, J., Ghosh, S., and Wang, L., 2018, "Efficient Robust Design Optimization Using Gaussian Process and Intelligent Sampling," *AIAA Paper No. 2018-4175*.
- [5] Bade, S., Wagner, M., Hirsch, C., Sattelmayer, T., and Schuermans, B., 2013, "Design for Thermo-Acoustic Stability: Modeling of Burner and Flame Dynamics," *ASME J. Eng. Gas Turbines Power*, **135**(11), p. 111502.
- [6] Bade, S., Wagner, M., Hirsch, C., Sattelmayer, T., and Schuermans, B., 2013, "Design for Thermo-Acoustic Stability: Procedure and Database," *ASME J. Eng. Gas Turbines Power*, **135**(12), p. 121507.
- [7] Aguilar, J. G., and Juniper, M. P., 2018, "Adjoint Methods for Elimination of Thermoacoustic Oscillations in a Model Annular Combustor Via Small Geometry Modifications," *ASME Paper No. GT2018-75692*.
- [8] Guo, S., Silva, C. F., Ghani, A., and Polifke, W., 2019, "Quantification and Propagation of Uncertainties in Identification of Flame Impulse Response for Thermoacoustic Stability Analysis," *ASME J. Eng. Gas Turbines Power*, **141**(2), p. 021032.
- [9] Ndiaye, A., Bauerheim, M., and Nicoud, F., 2015, "Uncertainty Quantification of Thermoacoustic Instabilities on a Swirled Stabilized Combustor," *ASME Paper No. GT2015-44133*.
- [10] Magri, L., Bauerheim, M., Nicoud, F., and Juniper, M. P., 2016, "Stability Analysis of Thermo-Acoustic Nonlinear Eigenproblems in Annular Combustors—Part II: Uncertainty Quantification," *J. Comput. Phys.*, **325**, pp. 411–421.
- [11] Mensah, G. A., Magri, L., and Moeck, J. P., 2017, "Methods for the Calculation of Thermoacoustic Stability Margins and Monte Carlo-Free Uncertainty Quantification," *ASME Paper No. GT2017-64829*.
- [12] Silva, C., Magri, L., Runte, T., and Polifke, W., 2016, "Uncertainty Quantification of Growth Rates of Thermoacoustic Instability by an Adjoint Helmholtz Solver," *ASME J. Eng. Gas Turbines Power*, **139**(1), p. 011901.
- [13] Bauerheim, M., Ndiaye, A., Constantine, P., Moreau, S., and Nicoud, F., 2016, "Symmetry Breaking of Azimuthal Thermoacoustic Modes: The UQ Perspective," *J. Fluid Mech.*, **789**, pp. 534–566.
- [14] Avdonin, A., Jaensch, S., Silva, C. F., Česnovar, M., and Polifke, W., 2018, "Uncertainty Quantification and Sensitivity Analysis of Thermoacoustic Stability With Non-Intrusive Polynomial Chaos Expansion," *Combust. Flame*, **189**, pp. 300–310.
- [15] Avdonin, A., and Polifke, W., 2018, "Quantification of the Impact of Uncertainties in Operating Conditions on the Flame Transfer Function With Non-Intrusive Polynomial Chaos Expansion," *ASME J. Eng. Gas Turbines Power*, **141**(1), p. 011020.
- [16] Clarich, A., and Russo, R., 2018, "Formulations for Robust Design and Inverse Robust Design," *Uncertainty Management for Robust Industrial Design in Aeronautics* (Notes on Numerical Fluid Mechanics and Multidisciplinary Design, Vol. 140), Springer, pp. 447–462.
- [17] Queipo, N. V., Haftka, R. T., Shyy, W., Goel, T., Vaidyanathan, R., and Kevin Tucker, P., 2005, "Surrogate-Based Analysis and Optimization," *Prog. Aerosp. Sci.*, **41**(1), pp. 1–28.
- [18] Komarek, T., and Polifke, W., 2010, "Impact of Swirl Fluctuations on the Flame Response of a Perfectly Premixed Swirl Burner," *ASME J. Eng. Gas Turbines Power*, **132**(6), p. 061503.
- [19] Tay-Wo-Chong, L., Bomberg, S., Ulhaq, A., Komarek, T., and Polifke, W., 2012, "Comparative Validation Study on Identification of Premixed Flame Transfer Function," *ASME J. Eng. Gas Turbines Power*, **134**(2), p. 021502.
- [20] Oberleithner, K., and Paschereit, C. O., 2016, "Modeling Flame Describing Functions Based on Hydrodynamic Linear Stability Analysis," *ASME Paper No. GT2016-57316*.
- [21] Albayrak, A., and Polifke, W., 2016, "Propagation Velocity of Inertial Waves in Cylindrical Swirling Flow," 23rd International Congress on Sound and Vibration (ICSV23), Athens, Greece, July 10–14, pp. 1–8.
- [22] Tay-Wo-Chong, L., Komarek, T., Kaess, R., Föller, S., and Polifke, W., 2010, "Identification of Flame Transfer Functions From LES of a Premixed Swirl Burner," *ASME Paper No. GT2010-22769*.
- [23] Poinso, T., 2017, "Prediction and Control of Combustion Instabilities in Real Engines," *Proc. Combust. Inst.*, **36**(1), pp. 1–28.
- [24] Hoeijmakers, M., Kornilov, V., Lopez Arteaga, I., de Goey, P., and Nijmeijer, H., 2014, "Intrinsic Instability of Flame-Acoustic Coupling," *Combust. Flame*, **161**(11), pp. 2860–2867.
- [25] Emmert, T., Bomberg, S., Jaensch, S., and Polifke, W., 2017, "Acoustic and Intrinsic Thermoacoustic Modes of a Premixed Combustor," *Proc. Combust. Inst.*, **36**(3), pp. 3835–3842.
- [26] Albayrak, A., Steinbacher, T., Komarek, T., and Polifke, W., 2017, "Convective Scaling of Intrinsic Thermo-Acoustic Eigenfrequencies of a Premixed Swirl Combustor," *ASME J. Eng. Gas Turbines Power*, **140**(4), p. 041510.
- [27] Candel, S., Durox, D., Schuller, T., Bourgoin, J. F., and Moeck, J. P., 2014, "Dynamics of Swirling Flames," *Annu. Rev. Fluid Mech.*, **46**(1), pp. 147–173.
- [28] Schneider, E., Staudacher, S., Schuermans, B., Ye, H., and Meeuwissen, T., 2007, "Real-Time Modelling of the Thermoacoustic Dynamics of a Gas Turbine Using a Gaussian Process," *ASME Paper No. GT2007-27468*.
- [29] Chattopadhyay, P., Mondal, S., Bhattacharya, C., Mukhopadhyay, A., and Ray, A., 2017, "Dynamic Data-Driven Design of Lean Premixed Combustors for Thermoacoustically Stable Operations," *ASME J. Mech. Des.*, **139**(11), p. 111419.
- [30] Chattopadhyay, P., Mondal, S., Ray, A., and Mukhopadhyay, A., 2018, "Dynamic Data-Driven Combustor Design for Mitigation of Thermoacoustic Instabilities," *ASME J. Dyn. Syst., Meas., Control*, **141**(1), p. 014501.
- [31] Lataniotis, C., Marelli, S., and Sudret, B., 2017, "UQLab User Manual—Kriging (Gaussian Process Modelling)," Chair of Risk, Safety and Uncertainty Quantification, ETH Zurich, Zurich, Switzerland, Report No. 3.
- [32] Rasmussen, C. E., and Williams, C. K. I., 2006, *Gaussian Processes for Machine Learning (Adaptive Computation and Machine Learning Series)*, The MIT Press, Cambridge, MA.
- [33] Jones, D. R., Schonlau, M., and Welch, W. J., 1998, "Efficient Global Optimization of Expensive Black-Box Functions," *J. Global Optim.*, **13**(4), pp. 455–492.
- [34] Forrester, A. I. J., and Keane, A. J., 2009, "Recent Advances in Surrogate-Based Optimization," *Prog. Aerosp. Sci.*, **45**(1–3), pp. 50–79.
- [35] Kwon, H., Choi, S., Kwon, J.-H., and Lee, D., 2016, "Surrogate-Based Robust Optimization and Design to Unsteady Low-Noise Open Rotors," *J. Aircr.*, **53**(5), pp. 1448–1467.
- [36] Ryan, K. M., Kristensen, J., Ling, L., Ghosh, S., Asher, I., and Wang, L., 2018, "A Gaussian Process Modeling Approach for Fast Robust Design With Uncertain Inputs," *ASME Paper No. GT2018-77007*.
- [37] Liu, H., Cai, J., and Ong, Y.-S., 2017, "An Adaptive Sampling Approach for Kriging Metamodeling by Maximizing Expected Prediction Error," *Comput. Chem. Eng.*, **106**(2), pp. 171–182.
- [38] Swiler, L., Slepoy, R., and Giunta, A., 2006, "Evaluation of Sampling Methods in Constructing Response Surface Approximations," *AIAA Paper No. 2006-1827*.
- [39] Loeppky, J. L., Sacks, J., and Welch, W. J., 2009, "Choosing the Sample Size of a Computer Experiment: A Practical Guide," *Technometrics*, **51**(4), pp. 366–376.
- [40] Silva, C. F., Pettersson, P., Iaccarino, G., and Ihme, M., 2018, "Generalized Chaos Expansion of State Space Models for Uncertainty Quantification in Thermoacoustics," Summer Program, Center for Turbulence Research, Stanford University, Stanford CA, June 24–July 20, pp. 339–348.
- [41] Ahmed, M. Y. M., and Qin, N., 2009, "Comparison of Response Surface and Kriging Surrogates in Aerodynamic Design Optimization of Hypersonic Spiked Blunt Bodies," 13th International Conference on Aerospace Sciences and Aviation Technology, Military Technical College, Cairo, Egypt, May 28–30, Paper No. ASAT-13-AE-15.
- [42] Audet, C., and Dennis, J., 2002, "Analysis of Generalized Pattern Searches," *SIAM J. Optim.*, **13**(3), pp. 889–903.
- [43] Goel, T., Vaidyanathan, R., Haftka, R. T., Shyy, W., Queipo, N. V., and Tucker, K., 2007, "Response Surface Approximation of Pareto Optimal Front in Multi-Objective Optimization," *Comput. Methods Appl. Mech. Eng.*, **196**(4–6), pp. 879–893.
- [44] Custódio, A., Madeira, J., Vaz, A., and Vicente, L., 2011, "Direct Multiobjective Search for Multiobjective Optimization," *SIAM J. Optim.*, **21**(3), pp. 1109–1140.
- [45] Saltelli, A., Ratto, M., Andres, T., Campolongo, F., Cariboni, J., Gatelli, D., Saisana, M., and Tarantola, S., 2008, *Global Sensitivity Analysis: The Primer*, Wiley, Hoboken, NJ.
- [46] Silva, C. F., Merk, M., Komarek, T., and Polifke, W., 2017, "The Contribution of Intrinsic Thermoacoustic Feedback to Combustion Noise and Resonances of a Confined Turbulent Premixed Flame," *Combust. Flame*, **182**, pp. 269–278.